Geophysical Research Letters

Supporting Information for

Thermal Pressure in the Laser Heated Diamond Anvil Cell: A Quantitative Study and Implications for the Density vs. Mineralogy Correlation of the Mantle

Connor Ethan Yen, Quentin WIlliams, and Martin Kunz

Contents of this File

Here we cover the exact experimental design, including the sample and Laser Heated Diamond Anvil Cell preparation, the specifics of the diffraction setup, and the computational methods of determining beam temperature. We also include here the mathematical derivation of our model.

Introduction

Section 1 covers the experimental design and Section 2 covers the derivation of our model; Section 3 derives the thermodynamic thermal pressure.

1 Experimental Design

1.1 Sample preparation

Experiments were performed on commercially available silver iodide, AgI (SIGMA-ALDRICH), and gem-quality San Carlos olivine, $(Mg_{0.9}^{2+}, Fe_{0.1}^{2+})_2SiO_4$. See S.I. Table 1 for thermoelastic parameters. Our choice of these two compounds is motivated both by each material having notably uniform and stable coupling with infrared laser heating, but also by the product of thermal expansion and bulk modulus (αK_0) of the two materials being almost equivalent (S.I. Table 1), while their strengths are expected to markedly differ. Accordingly, these two materials provide a means for experimentally demonstrating whether shear strength exercises a major role on thermal pressure, or whether thermal pressure is largely governed by the thermodynamics of local heating of a nearly isochoric system.

	AgI	San Carlos Olivine
Bulk Modulus (K_0)	42(2) GPa (1)	129.4(4) GPa (2)
dK/dP (K')	3.8(3) (1)	4.6(1) (2)
Thermal Expansion (α)	8 x 10^{-5}/K (3)	2.7(3) x 10^{-5}/K (4)
Anderson-Grüneisen Parameter (δ)	3.8(3)	4.6(1)
αK_0	3.36 x 10^{-3} GPa/K	3.49 x 10^{-3} GPa/K

S.I. Table 1: Thermoelastic parameters of AgI and San Carlos olivine at ambient pressure and temperature. (1) *Hull and Keen* [1999](2) *Liu et al.* [2005], (3) The value for NaCl was used as an approximation *Chauhan and Singh* [2007], (4) *Liu and Li* [2006]. The Anderson-Grüneisen Parameter was set equal to dK/dP: this assumes that the isothermal derivative with respect to volume of αK_T is negligible, and represents a good approximation for both halides and olivine [*Anderson*, 1997].

The samples were powdered using a mortar and pestle, and x-ray powder diffraction of the samples at modest pressures (2 – 4 GPa) and room temperature confirmed their chemical purity. High pressures were generated using a BX90 diamond anvil cell [*Kantor et al.*, 2012], with type 2a CVD diamonds ($400\mu m$ culets). Steel was used as the gasket material, which was pre-indented to a thickness of $100\mu m$, and laser drilled to yield sample chambers of $160\mu m$ in diameter. Before loading, parallel tungsten blocks were used to compact the powdered samples. To further reduce sample porosity, the gasket was loaded with the compacted sample, modestly pressurized (< 3 GPa), and then loaded with more sample. Initial cold pressures were determined to be 3-4 GPa for the AgI, and 2-3 GPa for the San Carlos olivine using R-line fluorescence on a cluster of ruby chips placed close to the center of the sample chamber [*Mao et al.*, 1986]. The samples were loaded without a pressure medium or thermal insulation material in order to keep artifacts due to insufficient geometric control of a multi-component sample assembly at a minimum. The lack of inclusion of a thermal insulation layer is justified in samples (like AgI and olivine) where the low thermal conductivity allows the sample in the center of the chamber to be robustly heated by the IR laser without draining its temperature through the diamond heat sinks. In essence, the sample layer in contact with the diamonds acts as the insulation layer for the bulk sample, and the sample itself therefore serves as its own thermal insulation layer. As shown by *Manga*

and Jeanloz [1996], the axial temperature gradients expected in a dielectric material have a negligible effect on the temperature deduced from the observed thermal radiation spectrum. Furthermore, the lack of any observable peak broadening or splitting within the hot powder diffraction patterns indicates that the axial thermal gradients are very steep, and therefore the cold insulation layer is too thin to affect the diffraction patterns and thus bias the deduced thermal pressures.

1.2 Synchrotron X-ray diffraction

Angle-dispersive in situ X-ray powder diffraction patterns at high pressure and high temperature were collected at beamline 12.2.2 at the Advanced Light Source at the Lawrence Berkeley National - Laboratory using an X-ray wavelength of $\lambda = 0.5166\text{Å}$ (24 keV) and $\lambda = 0.4969\text{Å}$ (25 keV) for the silver iodide and San Carlos olivine experiments, respectively. The X-ray energy for the AgI was lowered to 24 keV to be at a safe distance from the Ag-K-α-absorption edge. At each spatial position, X-ray diffraction patterns were taken both before and during the IR laser heating to yield ambient and heated diffraction patterns. The X-ray beam size was 10 μm. Patterns were collected with exposure times of 30 sec on a MAR3450 image plate. The detector distance and orientation were calibrated using a CeO_2 standard at the sample position.

1.3 Laser heating and temperature measurement

Laser heating of the LHDAC was conducted using a 1090 nm IR fiber laser system [*Kunz et al.*, 2018], with a beam size of $30\mu\text{m}$ FWHM in diameter. The silver iodide sample was heated with $0.9 - 1.0\text{W}$ in both the upstream and downstream directions. The San Carlos olivine sample was heated with powers of $2.5 - 3.2\text{W}$ upstream and $4.5 - 5.7\text{W}$ downstream. To probe the sample across the hot spot, the sample had to be moved relative to the stationary X-ray beam, and with it, the laser hot spot which in turn was kept centered on the gasket hole (see S.I. Figure 1).

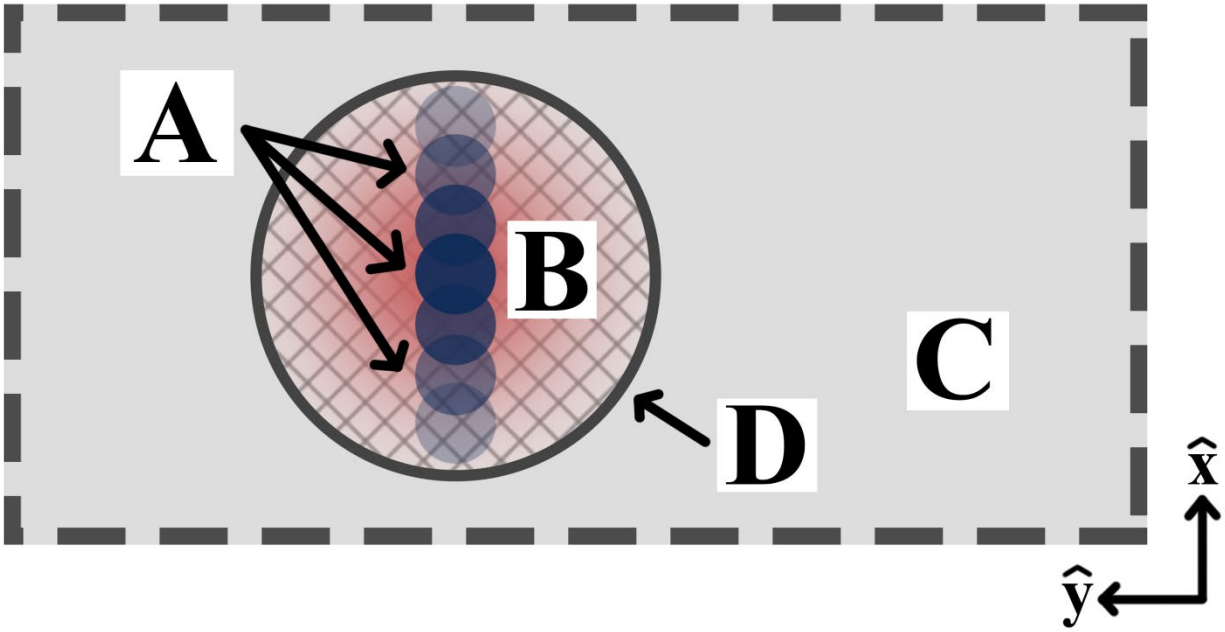

S.I. Figure 1: x-y cross section of the LHDAC as seen along the X-ray path. (A) X-ray beam positions (blue) across the diameter of the sample chamber. Note that the laser beam (red) is constantly centered at the origin of the sample space. (B) powdered sample

The center of the gasket hole served as the reference for positioning the laser hot spot. As a result, this procedure created an individual hot spot for every diffraction measurement. The laser heating set-up on beamline 12.2.2 [*Kunz et al.*, 2018] allows for quasi real-time temperature mapping of the sample chamber during a heating event. Temperatures were measured using the double sided spectroradiometric pyrometry set up on beamline 12.2.2, which employs a modified peak scaling approach [*Rainey and Kavner*, 2014]. This approach avoids the notorious chromatic aberration artifacts and also produces full absolute temperature maps in real time, thus enabling the spatial mapping of the thermal pressure effects presented here.

The pyrometry setup produces upstream and downstream 74μm x 74μm square temperature maps centered at the peak of the laser hotspot. As a result, radial temperature readings from the center of the sample exist from 0 to 37μm for the full azimuthal range, but disregarding radial completeness, temperature data exist from 0 to 52.3μm from the center. We plotted the upstream and downstream temperatures against radial distance by averaging the temperatures of pixels with the same Euclidian distance (within floating point error) from the center of the 74μm x 74μm temperature maps. The upstream and downstream graphs were averaged to produce an average temperature vs. radial distance plot.

Due to the large thermal conductivity of the diamond anvils, it has been shown that at the diamond/sample interface, the sample has a temperature close to room temperature [*Kiefer and Duffy*, 2005]. To construct the temperatures between 52.3μm and 80μm (the sample edge), we use a simple linear decrease between the points at $(44.5\text{um}, \text{avg}([T_{37um}, T_{52.3um}]))$ and $(80\text{um}, 298K)$. To construct the first point of the linear decrease, we considered the temperature points between 37μm and 52.3μm because 360-degree azimuthal averaging is only possible between 0 and 37μm. The average

distance and temperature of the points between 37μm and 52.3μm gives us the starting point for the linear decrease.

The average beam temperatures of sections centered between 0 and 47.3μm (52.3μm – 5μm) was obtained by averaging the corresponding 10μm section (our beam size) of the average temperature vs. radial distance graphs. Average beam temperatures of sections centered between 52.3μm and 80μm were obtained by taking the average temperature-value of the linear decrease over the corresponding 10μm radial section. The thus obtained experimental temperature spots were then fit with a Gaussian function (S.I. Table 1).

S.I. Table 1: Constants derived from a fit of a Gaussian function (T(r)=y_0+(A/(w√(π/2)))exp(-2((x-x_c)/w)^2)) to the temperature data.

	AgI	San Carlos Olivine
y_0	341(39)	356(37)
x_c	1.84 ± 1.42	-0.11± 0.84
w	50.3 ± 3.7	54.7 ± 2.7
A	642377 ± 60777	818137 ± 57077

1.4 Pressure Determination

For computational simplicity, we combine the Murnaghan Equation [*Murnaghan*, 1951] with the first order equation of thermal expansion through EosFit7 GUI [*Angel et al.*, 2014] for the PVT EOS (Equation 1).

Equation 1

$$P = \frac{K_0(1+\alpha\Delta T)^{-\delta}}{K'}\left(\left(\frac{V_P}{V_0(1+\alpha\Delta T)}\right)^{-K'} - 1\right)$$

Within the pressure range and volumetric strains that we probe, the Murnaghan equation is expected to provide a representation of the pressure-volume behavior of these materials that is comparable in accuracy to other, harder to invert finite strain equations of state. The expanded Murnaghan equation (Equation 1) requires observable input values for the initial (V_0, before heating) and final (V_P, during heating) sample unit cell volumes, and the temperature (ΔT) experienced by the probed sample volume, together with the physical constants K_0, K', α, and the Anderson-Grüneisen parameter δ [*Angel et al.*, 2014; *Helffrich and Connolly*, 2009]. Note that in this formulation we account for the temperature dependence of the bulk modulus through the Anderson-Grüneisen parameter δ, whereas no pressure or temperature dependence of the thermal expansivity α is included. This simple

formulation of α reflects that the relative roles of pressure and temperature on this parameter are of opposite sign, and the effect of modest variations in thermal expansion on volume are dwarfed by the pressure effects observed. With V_0 and V_P determined using the unit cell parameters from before and during the laser-heating, and ΔT determined from the temperature map produced by the pyrometry set up on beamline 12.2.2, Equation 1 yields the total pressure at every position of the X-ray/sample transect (S.I. Figure 1). To obtain the thermal pressure component P_{th}, we subtract the pressure obtained through Equation 1 at the corresponding position prior to the heating from that calculated at high temperatures (i.e. we subtract the pressure applied by the diamonds at ambient temperature).

Scattering intensity versus 2θ plots were obtained by azimuthal integration of the 2-dimensional powder diffraction patterns using DIOPTAS [*Prescher and Prakapenka*, 2015]. From the intensity versus 2θ plots for the silver iodide sample, lattice spacings with Miller indices (200), (220), (311), (222), (400), (420), and (422) were used to refine the unit-cell parameters of silver iodide's cubic crystal structure. From the intensity versus 2θ plots for the San Carlos olivine, lattice spacings with Miller indices (020), (021), (101), (002), (130), (131), (112), and (211) were analyzed using Celref 3 [*Laugier and Bochu*, 2002] to yield orthorhombic unit-cell parameters.

2 Model Construction

We limit our examination to the thermal pressure arising due to restrictions on the total volume. The construction of our model is as follows:

We reduce the sample chamber to a circular geometry, which we can then partition with the shell differential element. Consider the thermal pressure that arises at the differential element *r* (i.e. the region in the radial interval $[r - dr, r + dr]$). Considering this element consequently divides the entire sample into two regions: the interior – the region within the radial interval $[0, r - dr]$, and the exterior – the region within the radial interval $[r + dr, b]$ (where *b* is the radius of the entire sample).

Predicated by *Heinz* [1990], we estimate the temperature distribution with a Gaussian curve. As such, when we move farther away from the center of the sample, the temperature decreases. Thus, the thermal expansion of the interior region $[0, r - dr]$ occurs at a greater magnitude than that of the exterior region $[r + dr, b]$. If we hold the volume of the interior region constant, thermal pressure arises to counteract this thermal expansion according to the restriction. Similarly, holding the volume of the exterior region constant results in a smaller thermal pressure than that of the interior. Doing so lets us think of the *r*-shell as being incompressible – which translates to an infinite shear strength analogy. With this construction, the *r*-shell experiences a greater thermal pressure from the thermal expansion of the interior volume (which points radially outwards at the boundary $r - dr$) than the thermal pressure it experiences from the exterior (which points radially inwards at the boundary $r + dr$). Of course, in reality as $dr \to 0$, the greater interior thermal pressure would cause the interior volume to expand and thus equilibrate with the outer volume. However, modeling thermal pressure by isochorically restricting the interior volume represents a good upper bound.

With this framework in mind, we can derive a mathematical model. As mentioned above, we use a Gaussian curve to model the temperature distribution of the heated sample (Equation 2).

Equation 2

$$T(x) = T_0 + \left(\frac{A}{w\sqrt{\pi/2}}\right)\exp\left(-2\left(\frac{x - x_c}{w}\right)^2\right)$$

Note that Equation 2 is the area version of the Gaussian Equation. Most are familiar with the expression of the Gaussian as a function of the standard deviation (σ) and mean (μ), i.e.

Equation 3

$$g(x) = \frac{1}{\sigma\sqrt{2\pi}} e^{-\frac{1}{2}\left(\frac{x-\mu}{\sigma}\right)^2}$$

In Equation 2, x_c denotes the center of the curve (i.e. at x_c, $T(x_c)$ has its maximum), *A* denotes the area under the curve on the interval $[x_c - \sigma, x_c + \sigma]$, and *w* denotes the width of the curve on the interval $[x_c - \sigma, x_c + \sigma]$ which is 2σ. For conversions between *w* and common Gaussian parameters, see S.I. Table 2.

S.I. Table 2: Conversion matrix between different forms of Gaussian functions

σ, w	$\sigma = w/2$
FWHM, w	$\text{FWHM} = w\sqrt{2 \cdot \ln(2)}$
Height of the curve $(y_c - y_0)$	$\text{Height} = \frac{A}{w \cdot \sqrt{\pi/2}}$

Using the area version of the Gaussian function lets us fit our temperature data with the Levenberg-Marquardt iteration algorithm. With Temperature expressed as a function of radius, we can express the thermal expansion coefficient and the bulk modulus as functions of temperature. For the thermal expansion coefficient, we use Equation 4.

Equation 4

$$\alpha(r) = \alpha_0 + \alpha_1 T(r)$$

For the bulk modulus, we introduce the Anderson-Grüneisen parameter to link compressibility with thermal expansion (Equation 5).

Equation 5

$$K(r) = K_0\left(1 + \alpha(r)\Delta T(r)\right)^{-\delta}$$

In the following derivation of the bulk modulus as a function of radius, dV_0 represents the volume of the unheated shell (i.e. the radial interval $[r - dr, r + dr]$) and dV_T represents the thermal expansion of dV_0 under unconstrained conditions

$$K(dV_T) = K_0 \left(\frac{dV_0}{dV_T}\right)^{\delta}$$

$$K(r) = K_0 \left(\frac{dV_0}{dV_0(1 + \alpha(r)\Delta T(r))}\right)^{\delta}$$

Per the temperature curve, at a given *r*-shell, the interior region expands to some heated volume, and the sum of the thermal expansion of the heated interior shells (i.e. $\int_0^r dV_T$) is pressurized to match the isochoric assumption of the interior volume (i.e. $\int_0^r dV_P = \pi r^2$) (Equation 6 & Equation 7). We employ the thermal expansion equation to represent the volumetric expansion of each interior shell (i.e. $dV_T = dV_0\big(1 + \alpha(r)\Delta T(r)\big)$), and we use the Murnaghan equation (Equation 1) to model the pressure needed to compress the sum of the heated volumes to adhere to the isochoric restriction (Equation 8).

Equation 6

$$dV_P = dV_T \left(1 + \frac{K'}{K} P\right)^{-\frac{1}{K'}}$$

Equation 7

$$\pi r^2 = \int_r^0 dV_T \left(1 + \frac{K'}{K} P\right)^{-\frac{1}{K'}}$$

Equation 8

$$\pi r^2 = \int_0^r 2\pi x dx\big(1 + a(x)T(x)\big) \left(1 + \frac{K'}{K(x)} P_{th}\right)^{-\frac{1}{K'}}$$

Thus, Equation 8 presents an upper bound for the thermal pressure that arises at a radial distance *r*. Note that due to the steepness of the Gaussian temperature curve in our experiments, the thermal pressure of the interior region dominates the thermal pressure contribution at a given radius, so taking our upper bound results in a good estimate for real thermal pressure.

3 Thermal pressure in isochorically heated volume is equal to αKdT:

Thermal pressure in a fully constrained volume heated to temperature T is by definition given as Equation 9.

Equation 9

$$P_{th} = \left(\frac{\partial P}{\partial T}\right)_V dT$$

This can be rewritten using the chain rule as Equation 10.

Equation 10

$$\left(\frac{\partial P}{\partial T}\right)_V = \left(\frac{\partial P}{\partial V}\right)_T \cdot \left(\frac{\partial V}{\partial T}\right)_P$$

Since by definition $\left(\frac{\partial P}{\partial V}\right)_T = K_T$ and $\left(\frac{\partial V}{\partial T}\right)_P = \alpha_P$, it follows that in the thermodynamic limit thermal pressure.

$$\left(\frac{\partial P}{\partial T}\right)_V dT = K_T \alpha_P dT$$

Anderson, O. L. (1997), The volume dependence of thermal pressure in solids, *Journal of Physics and Chemistry of solids*, *58*(2), 335-343.

Angel, R. J., M. Alvaro, and J. Gonzalez-Platas (2014), EosFit7c and a Fortran module (library) for equation of state calculations, *Zeitschrift für Kristallographie-Crystalline Materials*, *229*(5), 405-419.

Chauhan, R., and C. Singh (2007), Equation of state and thermal expansivity of NaCl under high pressure and high temperature, *Physica B: Condensed Matter*, *387*(1-2), 352-357.

Heinz, D. L. (1990), Thermal pressure in the laser-heated diamond anvil cell, *Geophysical Research Letters*, *17*(8), 1161-1164.

Helffrich, G., and J. Connolly (2009), Physical contradictions and remedies using simple polythermal equations of state, *American Mineralogist*, *94*(11-12), 1616-1619.

Hull, S., and D. Keen (1999), Pressure-induced phase transitions in AgCl, AgBr, and AgI, *Physical Review B*, *59*(2), 750.

Kantor, I., V. Prakapenka, A. Kantor, P. Dera, A. Kurnosov, S. Sinogeikin, N. Dubrovinskaia, and L. Dubrovinsky (2012), BX90: A new diamond anvil cell design for X-ray diffraction and optical measurements, *Review of Scientific Instruments*, *83*(12), 125102.

Kiefer, B., and T. S. Duffy (2005), Finite element simulations of the laser-heated diamond-anvil cell, *Journal of Applied Physics*, *97*(11), 114902.

Kunz, M., J. Yan, E. Cornell, E. E. Domning, C. E. Yen, A. Doran, C. M. Beavers, A. Treger, Q. Williams, and A. A. MacDowell (2018), Implementation and application of the peak scaling method for temperature measurement in the laser heated diamond anvil cell, *Review of Scientific Instruments*, *89*(8), 083903.

Laugier, J., and B. Bochu (2002), CELREF V3: Cell parameters refinement program from powder diffraction diagram. Laboratoire des Matériaux et du Génie Physique, Institut National Polytechnique de Grenoble, France, edited.

Liu, W., J. Kung, and B. Li (2005), Elasticity of San Carlos olivine to 8 GPa and 1073 K, *Geophysical Research Letters*, *32*(16).

Liu, W., and B. Li (2006), Thermal equation of state of (Mg0. 9Fe0. 1) 2SiO4 olivine, *Physics of the Earth and Planetary Interiors*, *157*(3-4), 188-195.
Manga, M., and R. Jeanloz (1996), Axial temperature gradients in dielectric samples in the laser-heated diamond cell, *Geophysical research letters*, *23*(14), 1845-1848.
Mao, H., J.-A. Xu, and P. Bell (1986), Calibration of the ruby pressure gauge to 800 kbar under quasi-hydrostatic conditions, *Journal of Geophysical Research: Solid Earth*, *91*(B5), 4673-4676.
Murnaghan, F. D. (1951), *Finite deformation of an elastic solid*, John Wiley & Sons.
Prescher, C., and V. B. Prakapenka (2015), DIOPTAS: a program for reduction of two-dimensional X-ray diffraction data and data exploration, *High Pressure Research*, *35*(3), 223-230.
Rainey, E., and A. Kavner (2014), Peak scaling method to measure temperatures in the laser-heated diamond anvil cell and application to the thermal conductivity of MgO, *Journal of Geophysical Research: Solid Earth*, *119*(11), 8154-8170.